

Nonlinear space-time focusing and filamentation of annular femtosecond pulses in dielectrics

THOMAS E. LANIER^{1,*} AND JEREMY R. GULLEY¹

¹Department of Physics, Kennesaw State University, Kennesaw, GA, 30144

*Corresponding author: tlanier6@kennesaw.edu, telanier@gmail.com

Compiled February 12, 2016

Filamentation during simultaneous space-time focusing in bulk fused silica is investigated numerically. We model the use of a pair of concentric gratings to transform a common femtosecond laser pulse with Gaussian spatial profile into a radially chirped, annular beam shape that is focused into the bulk of silica by a lens. By varying the energy and/or time-chirp of the incident pulse, we capture the pulse dynamics and material response that yields material modification and damage in the nonlinear focus. The results show rich pulse dynamics, enhanced damage/modification site localization, and suggest novel approaches to laser machining of solids. © 2016 Optical Society of America

OCIS codes: (140.3390) Laser materials processing; (320.5520) Pulse compression; (320.2250) Femtosecond phenomena; (140.3300) Laser beam shaping.

Version of record located at: <http://dx.doi.org/10.1364/JOSAB.33.000292>

© 2016 Optical Society of America. One print or electronic copy may be made for personal use only. Systematic reproduction and distribution, duplication of any material in this paper for a fee or for commercial purposes, or modifications of the content of this paper are prohibited.

1. INTRODUCTION

The interplay between the nonlinear optical effects and linear-optical diffraction and dispersion of an intense laser pulse leads to filamentation, whereby the pulse tends to exhibit quasi-cyclic spatial collapse-expand-collapse behavior [1]. This spatial character arises from the competition between Kerr self-focusing and the defocusing due to both beam diffraction and the negative index modulation associated with an ionized medium [2]. The phenomenon is also subject to temporal reshaping due to linear dispersion and dispersion due to self-phase modulation, contributing to additional pulse dynamics such as pulse-splitting [3]. These and other nonlinear optical effects have been studied extensively for decades [4–7].

For good reason, filamentation is commonly studied for the case of the ubiquitous Gaussian beam shape with a simple pulse shape in time, and simple spatial phase that corresponds to standard focusing optics. Numerous studies have explored material modification and damage in transparent dielectrics due to such femtosecond pulses [8–15]. More recent studies have explored less traditional pulses that approximate Airy or Bessel spatial profiles, Airy time shapes, or some combination of these [16–20]. These waveforms are of interest because of their self-healing and/or non-diffracting properties. Bessel beams, in particular, have been studied for the purpose of extending filaments and/or material modification sites [21–23].

Another facilitator of novel laser applications is obtained from spatially chirped pulses. For example, by angularly dispersing the frequency components of a laser pulse (via diffraction gratings, for example), and recombining them gradually (using a lens, for example), the Fourier limits of spatial and temporal compression may be synchronized at a target (the focus of the lens, for example). This is called simultaneous space-time focusing (SSTF) [24, 25] and has been used to control and shorten the extent of a high-intensity focal region, thus suppressing out-of-focus nonlinear optical effects [26–30]. This control has led to applications of SSTF laser writing on the back surface of fused silica samples [31], the demonstration of non-reciprocal laser writing in fused quartz [32], and better control over tissue ablation in the context of laser surgery [33].

The use of concentric-circle gratings for detection of planar displacements in the context of microlithography dates back 20 years [34] and is still developing [35]. Recently, concentric-circle gratings have been used to achieve superresolution imaging [36]. Electron beam lithography may be used with precision much better than 0.5 μm to fabricate circular Dammann gratings, which are concentric-circle gratings with variable pitch [37, 38]. In addition, femtosecond pulse-induced form birefringence [39] has been used to fabricate Fresnel zone plates with rings as narrow as 6.4 μm [40]. These advances speak not only to the technological viability of using concentric gratings, but also to the relevance of current research on novel schemes

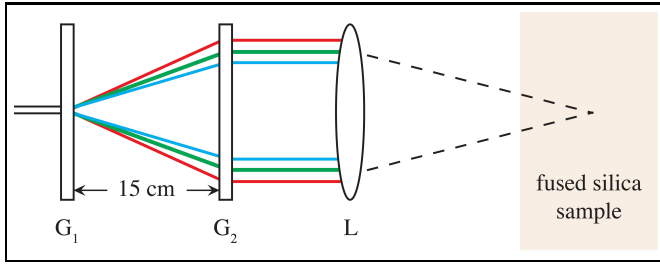


Fig. 1. Schematic of the simulated SSTF system comprising two concentric gratings G_1 and G_2 with ring spacing $d = 10 \mu\text{m}$ and a lens of focal length $f = 200 \text{ mm}$.

for the laser machining of solids.

Theoretical treatments of SSTF are often concerned mainly with the Fourier synthesis of the pulse as it propagates. The propagation is treated linearly because Fourier superposition is linear, and optical nonlinearities are effectively confined to the focal region. However, an investigation concerned with the microscopic, quantitative details of the material modification and pulse evolution at the focus requires inclusion of the nonlinear contributions to propagation.

In this paper, we numerically investigate radially-chirped annular beams via simulated propagation of time-chirped femtosecond pulses through the optical system shown in Fig. 1. This system consists of an ordinary lens preceded by a pair of concentric gratings. By dispersing the spectral content of the input pulse into all 2π radians of the transverse plane, the temporal defocusing between gratings is accompanied by radial spatial spreading, as opposed to spatial spreading along a line in the transverse plane as in standard SSTF via linear gratings. In this way, the gradient of the peak intensity of the space-time-focusing pulse after the lens is increased relative to standard SSTF via linear gratings (all other things being equal). The highly nonlinear focusing of this annular pulse may be expected to produce space-time-evolution that deviates significantly from established results for Bessel-like beam shapes. We first specify and briefly describe the spectral numerical propagation formalism used in this paper. Second, we present and interpret a model for concentric gratings suited to the spectral propagation code. Next, we establish a basis for our study of annular SSTF in fused silica in terms of annular SSTF in vacuum. Finally, we present an investigation of the evolution of annular SSTF pulses and the associated plasma-induced material modification in fused silica for various pulse energies and shapes, the latter of which is tuned by the time-chirp of the input pulse.

2. THEORETICAL FORMALISM

A. Propagation Scheme

We numerically investigate simultaneous space-time focusing (SSTF) of radially-chirped annular beams corresponding to the system shown in Fig. 1. Our simulations compute the laser pulse propagation in the retarded-time reference frame by numerically solving the unidirectional pulse propagation equation (UPPE) in cylindrical coordinates [41]:

$$\begin{aligned} \partial_z E(k_\perp, \omega, z) = ik_z E(k_\perp, \omega, z) + \\ + \frac{i\omega^2}{2\epsilon_0 c^2 k_z} P^{\text{NL}}(k_\perp, \omega, z) - \frac{\omega}{2\epsilon_0 c^2 k_z} J(k_\perp, \omega, z). \end{aligned} \quad (1)$$

Here, $k_z = \sqrt{k^2(\omega) - k_\perp^2}$ is the z -component of the wave vector with magnitude $k(\omega) = n(\omega)\omega/c$, ϵ_0 is the permittivity of free space, and the complex electric field array $E(k_\perp, \omega, z)$ is stored at discrete spatial frequencies k_\perp and angular frequencies ω . This non-paraxial spectral propagation scheme possesses the feature that linear propagation is exact within the limits of the accuracy of the linear refractive index $n(\omega)$ and the unidirectional approximation [42]. The evolution equation for spectral amplitudes A , related to E by $E(k_\perp, \omega, z) = \exp(ik_z z)A(k_\perp, \omega, z)$, is a set of ordinary differential equations, which we solve using a fourth-order Runge-Kutta library with adaptive stepping capabilities.

During each z step, inverse spectral transforms take $E(k_\perp, \omega, z)$ from $\omega \rightarrow t$ and from $k_\perp \rightarrow r$ to calculate the nonlinear source terms during each z step. The former is accomplished by a standard fast Fourier transform. In cylindrical coordinates the latter is accomplished via the Hankel transform [43–45], which is performed by multiplication by a self-reciprocal matrix (see Appendix A).

In the fused silica sample, we calculate the nonlinear polarization at a particular position (r - and z -dependence suppressed) as

$$P^{\text{NL}}(t) = 2n_0\epsilon_0 n_2 \left[(1 - \alpha) I(t) + \alpha \int_{-\infty}^t R(t - \tau) I(\tau) d\tau \right] E(t), \quad (2)$$

where $I = \frac{1}{2}n_0\epsilon_0 c |E|^2$, n_0 is the linear refractive index at the pulse center frequency ω_0 , n_2 is the nonlinear refractive index, and $R(t)$ is the Raman response function with fraction $\alpha = 0.18$ [42]. The free current density J at each r is calculated by integrating the following coupled equations during each z step as described in [42]:

$$\frac{dJ}{dt} + \frac{J}{\tau_c} = \frac{q^2}{m} \rho E \quad (3)$$

$$\frac{d\rho}{dt} = W_{\text{PI}}(|E|) \left(1 - \frac{\rho}{\rho_n} \right) + W_{\text{aval}}(I)\rho \quad (4)$$

Here, ρ is the density of free charge carriers, $W_{\text{aval}} = \sigma I / E_g$ is the ionization rate due to avalanching, $\sigma = q^2 / (\epsilon_0 n_0 m c) \times \tau_c / (1 + \omega_0^2 \tau_c^2)$ is the cross section for inverse bremsstrahlung, W_{PI} is the photoionization rate calculated from the Keldysh model [46] as in [13], and all other parameters are defined in Table 1. The maximum densities $\rho_{\text{max}}(r, z)$ reached during the pulse time window are often regarded as a predictor in the context of laser machining/material modification studies [13, 47]. Our calculations of these "ionization tracks" are shown in Sections 3 and 4.

These nonlinear source terms produce the rich collection of effects that contribute to filamentation of intense laser pulses. For the case of a carefully constructed spatially chirped pulse, a band-limited, shortest-duration pulse is Fourier-synthesized by virtue of the space-time overlap of the pulse frequency content at the focus. The distribution of optical energy in space and time evolves toward the distribution that is maximally compressed in both dimensions simultaneously, even in vacuum. In the linear optical regime of bulk fused silica, the same can be true as long as chromatic dispersion of the pulse spectrum is corrected for in the construction of the initial pulse. The impact of nonlinear propagation and plasma generation occurring in such a system is the primary focus of this paper. Propagation between optical elements is assumed to be linear and is

therefore accomplished by multiplying $E(k_{\perp}, \omega, z)$ by the linear propagator $\exp(ik_z \Delta z)$. Recall that k_z is a function of ω and k_{\perp} . The optical components are treated as r - and ω -dependent transformations that act on $E(r, \omega)$. Thus, propagation through the system in Fig. 1 to the sample surface amounts to a sequence of ~ 7 non-commuting transformations that act on the pulse field array. This simulation scheme is capable of capturing subtle/realistic linear-optical effects that modify the pulse en route to the sample surface, and accomodates a wide variety of input pulses. The transformations for the optical components are described in the following sections.

B. Preparation of the Incident Field

In the system shown in Fig. 1, a radially chirped collimated annular beam is produced by a conjugating pair of concentric gratings. To model the action of concentric gratings on pulses incident upon them, we devise a transformation for converting an incident field to an output field corresponding to the m^{th} diffraction order. This may be done for the case of a linear-groove grating by transforming into new spatial frequencies [48]. In Cartesian coordinates, and diffracting into the x -direction, for example, this amounts to multiplying $E(x, \omega)$ by a phase whose argument is linear in x and linear in angular frequency ω . In cylindrical coordinates, manipulations via Hankel transform (HT) are subject to the properties of the Bessel functions that form its basis, and these functions do not factor as do exponentials. We circumvent this feature of modeling the action of a concentric grating on field data represented in cylindrical coordinates by employing a generalized Hankel shift [49, 50]:

$$\begin{aligned} F(k|\Delta k) &= \int_0^{\infty} f(r) J_0(r\Delta k) J_0(kr) r dr \\ &= \text{HT} [f(r) J_0(r\Delta k)] \end{aligned} \quad (5)$$

Here, $F(k|\Delta k)$ denotes the Hankel transform space representation of the function $f(r)$ after a shift of its spatial frequencies by Δk . Using the self-reciprocal property of the Hankel transform, the field $E'(r, \omega)$ after having been shifted to new spatial frequencies $k'_{\perp} = k_{\perp} + \Delta k$ is

$$E'(r, \omega) = \text{HT} [E(k_{\perp}, \omega|\Delta k)] = E(r, \omega) J_0(r\Delta k). \quad (6)$$

Here, $\Delta k = \Delta k(\omega)$ describes the angular dispersion imparted by the concentric grating and remains to be specified.

Table 1. Parameters used in simulations.

Symbol	Description	Value	Unit
n_0	Linear refractive index	1.453	
n_2	Nonlinear ref. index	3.00×10^{-20}	m^2/W
E_g	Band gap energy	9.00	eV
m	Reduced e-hole mass	7.834×10^{-31}	kg
τ_c	Free electron coll. time	1.00×10^{-15}	s
ρ_n	Max. plasma density	2.20×10^{28}	m^{-3}
q	Elementary charge	1.602×10^{-19}	C
ϵ_0	Vacuum permittivity	8.854×10^{-12}	F/m
c	Speed of light	2.998×10^8	m/s

We follow [48, 51] and expand the angular spread after the grating $\Delta\theta$ to first order in the incident angular spread $\Delta\gamma$ and angular frequency shift $\Delta\omega = \omega - \omega_0$:

$$\Delta\theta = \alpha \Delta\gamma + \beta \Delta\omega, \quad (7)$$

where the partial derivatives

$$\alpha \equiv \frac{\cos \gamma_0}{\cos \theta_0} \quad \beta \equiv \frac{-m \lambda_0^2}{2\pi d c \cos \theta_0} \quad (8)$$

are derived from the grating equation, with m and d denoting the particular diffraction order and groove spacing, respectively. The subscript 0 refers to a ray representing the path taken by, and wavelength of, the center frequency ω_0 . In terms of these angular spreads, the transverse components of the wave vectors before and after the concentric grating are written as

$$\begin{aligned} k_{\perp} &= k_0 \sin(\gamma_0 + \Delta\gamma) \approx k_0 (\sin \gamma_0 + \cos \gamma_0 \Delta\gamma) \\ k'_{\perp} &= k_0 \sin(\theta_0 + \Delta\theta) \approx k_0 (\sin \theta_0 + \cos \theta_0 \Delta\theta). \end{aligned} \quad (9)$$

This leads to

$$k'_{\perp} - k_{\perp} = \Delta k(\omega) = \frac{2\pi m}{d} \left(2 - \frac{\omega}{\omega_0} \right), \quad (10)$$

where sines of the 0th-order ray angles have been eliminated using the grating equation. We note that the preceding discussion bypasses a meticulous consideration of sign conventions associated with the grating equation, often written as $\sin \gamma + \sin \theta = m\lambda/d$. See Ref. [52] for a concise statement of these conventions.

Equations 6 and 10 constitute a concentric grating transformation useful for any incident field $E(r, \omega)$ (or $E(k_{\perp}, \omega)$) for which the expansion in Eq. 7 is appropriate. Systems involving higher harmonics that would not diffract into angles near θ_0 , or those involving multiple crossed laser beams would require suitable filtering/superpositions not described here. Throughout this paper, we choose $d = 10 \mu\text{m}$ and $m = 1$ in Eq. 10 to correspond to the first conical diffraction order.

Taking the electric field incident upon concentric grating G_1 to be a collimated beam apodized by a function $A(r)$ with complex spectrum $S(\omega)$, i.e., $E(r, \omega) = A(r) S(\omega)$, the frequency superposition $\int_{-\infty}^{\infty} E'(r, \omega) \exp(-i\omega t) d\omega$ has the form of an apodized Bessel beam at $z = 0$ [53, 54]:

$$E'(r, t) = \int_{-\infty}^{\infty} S(\omega) A(r) J_0(r\Delta k) e^{-i\omega t} d\omega \quad (11)$$

Thus, in its role as G_1 , the generalized Hankel shift produces an apodized frequency superposition of Bessel beams with axicon angles varying with frequency ω according to Eq. 10. In this paper we choose a Gaussian apodizing function $A(r) = \exp(-r^2/w^2)$. This corresponds to taking the spatial beam profile of the pulse incident upon G_1 to be a collimated Gaussian with $1/e^2$ intensity width w_{inc} . Throughout this paper, we choose $w_{\text{inc}} = 2 \text{ mm}$. As for $S(\omega)$, we will generally choose a simple Gaussian pulse specified in the time domain. The pulse is then modified in the frequency domain to effect a chirp in time prior to G_1 . This chirp will be varied for optimal space-time focusing of the annular pulse at the focus of the lens. Throughout this paper, we choose center wavelength $\lambda_0 = 800 \text{ nm}$ and initial pulse width (FWHM of the intensity) $\tau_0 = 40 \text{ fs}$.

As the field given by Eq. 11 is propagated by the UPPE method (with nonlinear source terms excluded to correspond

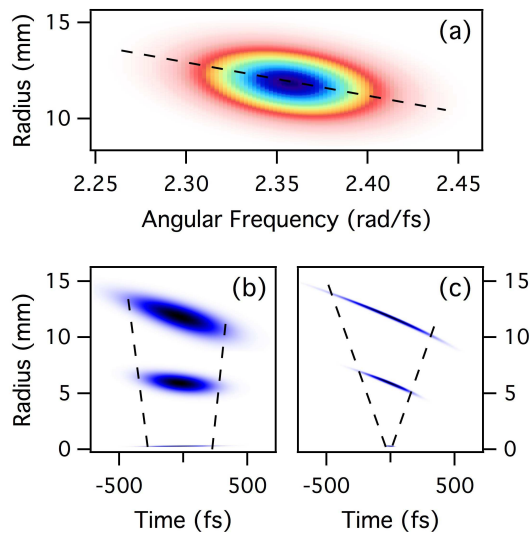


Fig. 2. SSTF in vacuum of $1\text{-}\mu\text{J}$ annular pulses arising from radial chirp. (a) Tilted $r\omega$ -spectrum just after G_2 . (b)-(c) Normalized intensities at various z -positions (superposed). In each case, propagation distances as measured from the $f = 200$ mm lens are 0 mm (top), 100 mm (middle), and 195 mm (bottom). (b) The initially bandwidth-limited 40 fs pulse. Peak intensities (TW/m^2) are 0.014 (top), 0.055 (middle), and 25.0 (bottom). (c) The positively pre-chirped 365 fs pulse. Peak intensities (TW/m^2) are 0.11 (top), 0.45 (middle), and 190 (bottom). Dashed lines are a guide for the eye.

to linear-optical propagation), an annular spatial dependence of the intensity develops as the pulse is angularly dispersed. At the same time, radial spatial chirp develops and the $r\omega$ -spectrum tilts such that lower frequencies are concentrated in the outer spatial wing and higher frequencies are pulled radially inward as the pulse approaches the z -position of G_2 . Throughout this paper, we place G_2 a distance 150 mm behind G_1 .

At G_2 , the spatial frequencies are shifted back to correspond to the collimated state by an additional application of the grating transformation Eqs. 6 and 10. However, bearing in mind that $J_0(x)$ is an even function, the transformation produces a pair of conical waves diffracted into either side of the incident cone direction ($m = 0$). The mathematics here can be interpreted by analogy with the description of sum- and difference-frequency generation in the context of elementary nonlinear optics: The oscillations in r imparted to $E(r, \omega, z_{G_1}) \rightarrow E'(r, \omega, z_{G_1})$ at G_1 by multiplication by $J_0(r\Delta k)$ essentially retain their period as the annulus opens during propagation along z . At G_2 , the multiplication is repeated, so that (suppressing ω) the product $J_0(r\Delta k) E'(r, z_{G_2})$ acquires oscillatory behavior $\sim \cos(\Delta kr) \exp(i(\Delta kr + \phi)) = \exp(i(2\Delta kr + \phi)) + \exp(i\phi)$, redistributing the energy into a component at $k_\perp \sim 0$ ("the zero-frequency signal") and a component at $k_\perp \sim 2\Delta k$ ("the second harmonic signal"). The latter is easily filtered after a HT to (k_\perp, ω) -space for this purpose. Experimentally, this would correspond to blocking the outer, non-collimated diffraction order. After G_2 , the field represents the collimated, radially chirped, annular pulse whose as of yet unspecified complex spectrum $S(\omega)$ at the input of G_1 is arbitrary as previously discussed with

respect to Eq. 7.

All propagation up to this point has been presumed linear. The total pulse energy will be set before entering the nonlinear sample, so as to correspond to a laboratory energy measurement somewhere after the lens. Consideration of how the single conical diffraction order should be scaled to satisfy conservation of energy is therefore unnecessary. We note that a blaze function $B(k_\perp)$ may be applied to $E'(k_\perp, \omega)$ after each grating to account for a dependence of grating efficiency on exit angle. In this paper, we choose $B(k_\perp) = 1$, corresponding to a grating blaze that diffracts the pulse spectrum uniformly. We also note that, while this paper models a conjugating pair of gratings, the described approach is not limited to the use of equal groove spacings d for each grating.

To simulate the action of an ordinary lens, the field $E(r, \omega)$ is transformed at the z -position of the lens by multiplication by a r - and ω -dependent phase (see Appendix B). This produces the curved phase and pulse fronts of the field transmitted by the lens, and accounts for spatially dependent group velocity dispersion and chromaticity of the lens to infinite dispersion order. This field is then propagated to the sample location. Throughout this paper, we choose a lens focal length of 200 mm, and place the sample surface 150 mm from the lens position.

SSTF of a broadband pulse occurs, even in vacuum, provided the frequency components are properly arranged in space and time. Figure 2 shows a preliminary illustration of SSTF, where two $1\text{-}\mu\text{J}$ pulse intensities are plotted for various z -positions between the lens and its geometric focus. Figure 2 (a) shows the shift in pulse spectrum vs. radius for the pulse at the lens position. Figure 2 (b) shows an initially unchirped 40 fs pulse as it focuses after traversing the system shown in Fig. 1. In Fig. 2 (c), the initial pulse has had a phase $\exp(ib_2(\omega - \omega_0)^2)$, with $b_2 = 2618 \text{ fs}^2$, applied to $E(r, \omega)$ prior to the first grating to correspond to the output of a standard pulse stretching device. This positively chirps the original pulse in time from $\tau_0 = 40$ fs to $\tau_0 = 365$ fs without changing its frequency content and effectively pre-compensates for the optical path difference of its frequencies between G_1 and G_2 . This parameter will be referred to as the "pre-chirp". For this case (Fig. 2 (c)), the collimated annulus after G_2 is essentially time-compressed (not shown). The radially-dependent optical path constituted by the lens spreads energy out in time as it directs it toward the focal point. Subsequently, a near-bandwidth-limited 43.75 fs pulse is gradually Fourier-synthesized by virtue of the increasing spatial overlap of its spectral content as it approaches the focus. What matters most is that the z -gradient of the optical power density may be increased significantly relative to ordinary spatial focusing provided an appropriately tuned pre-chirp, and that material dispersion is not required for this to occur.

On the other hand, if a dispersive sample is placed at a sample position appropriate for bulk material modification, linear dispersion may be compensated by adjusting the pre-chirp. Assuming normal dispersion is to be compensated for in the sample, decreasing the pre-chirp under-compensates for the path differences between gratings resulting in a collimated annulus after G_2 that is not time-compressed, as contrasted with the situation previously discussed and shown in Fig. 2 (c). In other words, such pulses prepared for modification in the bulk have intensity distributions that tend toward those in Fig. 2 (b), yet are maximally space- and time-compressed at focus by construction, at least in the regime of linear optics. It follows that linear dispersion occurring during the approach to a focus in

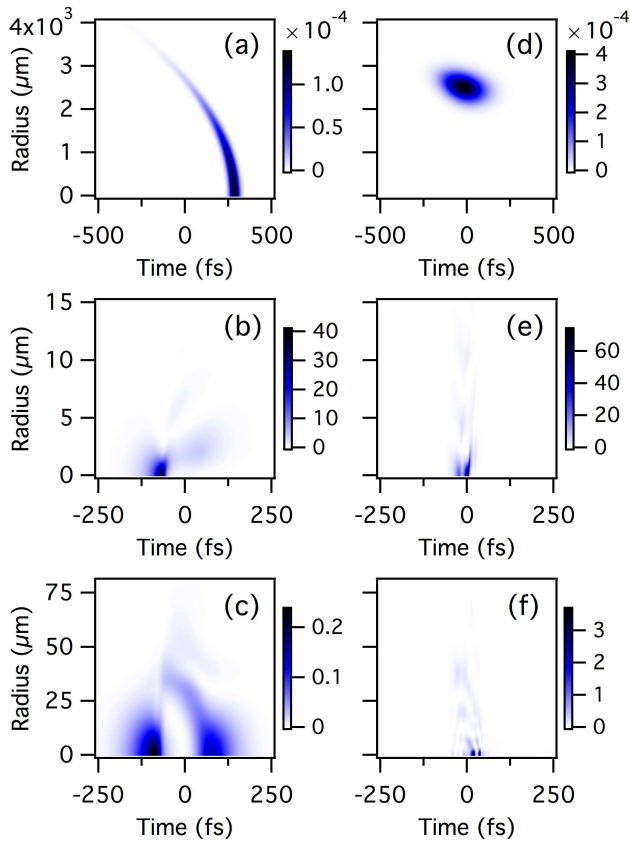


Fig. 3. Progression of the intensity (TW/cm^2), as $0.7\text{-}\mu\text{J}$ pulses pass through their nonlinear focus. Left column: Case GB. Right column: Case RCA with $b_2 = 1100 \text{ fs}^2$ ($\tau_0 = 158 \text{ fs}$). z -positions as measured from the sample surface are (a) 10 mm, (b) 72.65 mm, (c) 73.35 mm, (d) 10 mm, (e) 72.15 mm, (f) 72.90 mm.

the bulk of the sample enhances the z -gradient of the optical power density of a properly pre-chirped pulse. However, nonlinear optical processes play an increasing role in the propagation as the pulse annulus closes on itself and compresses in space as well as time. This may be expected to lead to filamentation characterized by dynamics and features distinct from the filamentation of more standard ultrashort laser sources. The next section describes simulations of the filamentation of radially chirped annular pulses in bulk fused silica and the resulting ionization tracks that are used as a metric for material modification and/or damage.

3. NUMERICAL SIMULATIONS

In these simulations, the pulse transmitted by the lens is first vacuum-propagated to the sample surface. As discussed above, the parameter b_2 may be modified for optimal SSTF to account for dispersion occurring as the pulse travels from the sample surface to the focal region. Since the inter-grating path difference corresponds to negative dispersion, and since fused silica exhibits normal dispersion in the chosen wavelength region, the positive parameter b_2 should be set $< 2618 \text{ fs}^2$ (the value that yielded optimal SSTF in vacuum), depending on focal region depth.

We place the sample surface 50 mm in front of the geometric

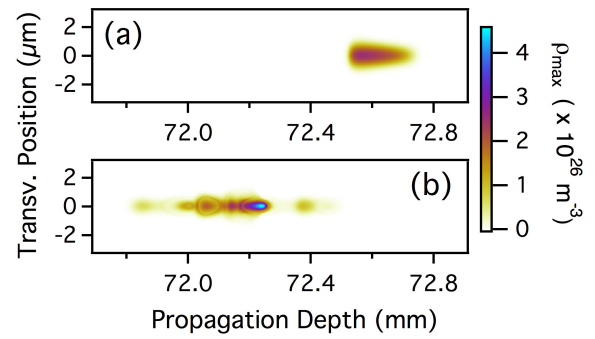


Fig. 4. Ionization tracks from $0.7\text{-}\mu\text{J}$ pulses corresponding to the two simulations depicted in Fig. 3. (a) Case GB. (b) Case RCA with $b_2 = 1100 \text{ fs}^2$ ($\tau_0 = 158 \text{ fs}$). The color map is set by the peak of the RCA data.

focus of the lens. This rather large depth was chosen in order to provide a clear picture of SSTF entirely within the sample, and devoid of sudden, though physically realistic, spikes in the Kerr nonlinearity at the sample surface. Similar depths have been investigated in the context of back-surface material modification studies [31]. In a preliminary investigation we find that, if all nonlinearities are neglected (switched off), then the space-time-focusing annular pulse is essentially fully time-compressed at the linear focus for $b_2 = 1100 \text{ fs}^2$, which corresponds to an incident pulse positively time-chirped to $\tau_0 = 158 \text{ fs}$. We focus our attention on the energy regime relevant to laser machining of dielectrics, which is on the order of 10^{-6} J .

We will refer to the Radially Chirped Annulus resulting from simulated propagation through the system in Fig. 1 as RCA. We use as a reference for comparison an ordinary Gaussian Beam with equal numerical aperture, referred to as GB. For the latter, the corresponding electric field at the sample surface is constructed by backwards-propagating the field at the vacuum focus back to the z -position of the sample surface. This corresponds to optimized GB focusing by an achromatic doublet. The result is then propagated forward in the fused silica sample toward the nonlinear focus. We define the numerical aperture of the RCA as r_0/f , where $r_0 = 11.834 \text{ mm}$ is the radial position of the intensity peak of the RCA immediately after the lens transformation. Equating this with $\lambda_0/\pi w_0$ for the GB yields a beam waist $w_0 = 4.304 \mu\text{m}$. The numerical aperture used throughout this paper is ~ 0.06 .

Here, it is useful to point out a few of the spatial characteristics of these pulses: As an annular intensity distribution is focused by a lens, its off-axis spatial width shrinks as it closes onto the propagation axis. In other words, "the ring gets thinner" as it "gets smaller". This is to be contrasted with a Gaussian beam, whose intensity maximum is always on-axis. Additionally, the GB possesses the feature that the underlying (linear-optical) spatial distributions have the same form in each Fourier plane. In other words, the spatial Fourier transform of a Gaussian is another Gaussian. By contrast, an annular intensity distribution becomes a Bessel-like distribution in the focal region. While these features will be perturbed significantly by optical nonlinearities, it is instructive to note that these distinctions are linear in nature from the start.

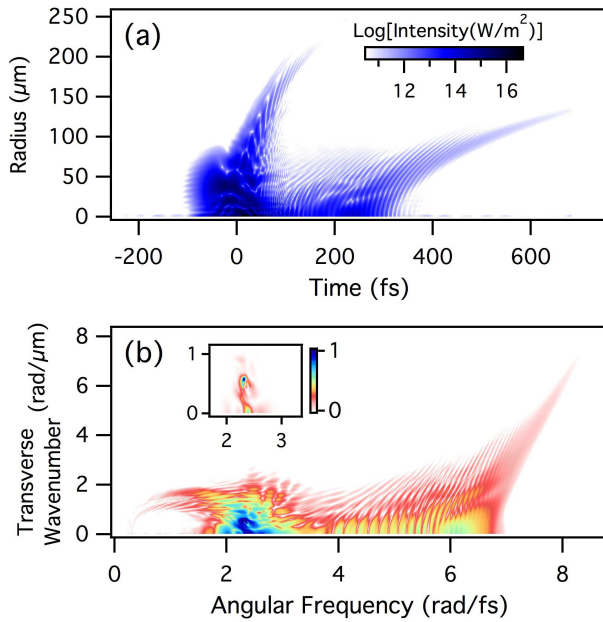


Fig. 5. The pulse beyond the nonlinear focus ($z = 72.90$ mm) for the $0.7\text{-}\mu\text{J}$ RCA with $b_2 = 1100$ fs² ($\tau_0 = 158$ fs). This pulse is also represented in Fig. 3-f. In each log plot, color maps range down to a factor of 10^{-6} of the peak. (a) The log of the intensity (W/m^2) in rt -space. (b) Normalized intensity (inset), and the log of the normalized intensity in $k_{\perp}\omega$ -space. The progression of this spectrum during propagation through the nonlinear focus is depicted in Visualization 1 (see Supplementary Material).

4. RESULTS

We first consider the case of a $0.7\text{-}\mu\text{J}$ RCA constructed using $b_2 = 1100$ fs² ($\tau_0 = 158$ fs), and compare it with a GB with pulse width $\tau_0 = 40$ fs and equal energy. The latter corresponds to a pulse that has bypassed the stretching device corresponding to b_2 , and with the grating pair replaced by a reflective telescope that increases the $1/e^2$ beam radius w by a factor of ~ 6 .

Figure 3 depicts the progression of the pulse intensity in rt -space for GB and RCA. Each three-pane sequence shows the pulse at z -positions "before, during, and after" the nonlinear focus, which occurs at different locations for reasons described below. Here, "after" was chosen to be 650 μm beyond the peak free carrier density for each case. Note that radius and time axes may vary from pane to pane in this figure.

We now describe the GB case. Panes (a)-(c) of Fig. 3 show the well-known pulse splitting that occurs in the focal region as plasma is generated and filamentation occurs [1, 3]. The free carrier-induced refractive index decrease arrests the spatial collapse due to Kerr self-focusing, and energy local to the early-time pulse wing is temporally advanced in the retarded frame. At the same z -position, energy in the late-time pulse wing partially diffracts away from the propagation axis, but remains sufficiently intense for subsequent Kerr re-focusing. For higher pulse energies, these effects occur before the entire spatial extent of the pulse reaches the filament. The net effect is that the front of the pulse partially shears apart from its temporal rear. The quasi-stable balance of Kerr, plasma, and ordinary beam diffraction effects is thus accompanied by the establishment of an intensity distribution with multiple maxima in time.

Panes (d)-(f) of Fig. 3 depict the analogous progression of the RCA. As the pulse approaches the focus, its off-axis spatial width, and owing to SSTF its time width, decrease as the annulus closes onto the propagation axis. In other words, the distribution in Fig. 3 (d) becomes narrower in both r and t dimensions as energy converges on $r = 0$. In the nonlinear focus, Kerr nonlinearity distorts the outer rings of the Bessel-like distribution and its central maximum, where appreciable plasma generation is essentially confined for this $0.7\text{-}\mu\text{J}$ case. The process of filamentation thus develops as a complex interplay between free-carrier-induced time-advance of on-axis energy, Kerr re-focusing, and deposition of additional energy to the propagation axis from the distorted spatial wing.

Shown in Fig. 4 are ionization tracks resulting from the $0.7\text{-}\mu\text{J}$ GB and RCA simulations of Fig. 3. The peak free carrier density produced by the RCA is seen to be larger than that of the GB by a factor of ~ 2 . In addition, the RCA track is more structured, and has a more localized peak structure, which occurs at $z \sim 72.2$ mm. Taking the free carrier density as a measure, the RCA is seen to come to a nonlinear focus earlier than the GB. We attribute this shift to the working definition chosen for numerical aperture of the RCA. In other words, lacking a precise definition for the case of a focusing annulus, the correspondence between its numerical aperture and that of a Gaussian beam is expected to be imperfect. It is to this ambiguity that we attribute the discrepancy between nonlinear focus depths.

Shown in Fig. 5 are logarithmic intensities corresponding to Fig. 3 (f) represented in real space ((r, t) - pane (a)) and spectral domains ((k_{\perp}, ω) - pane (b)). Note that the $k_{\perp}\omega$ -spectrum has been normalized for simplicity. Also, shown in the inset of Fig. 5 (b), is the same $k_{\perp}\omega$ -spectrum on a linear scale. Before the nonlinear focus, the $k_{\perp}\omega$ -spectrum is concentrated around a point where $k_{\perp} \sim 0.5$ rad/ μm . In other words, the focusing annulus contains no energy traveling parallel to the propagation axis, which is to be contrasted with the GB case. This attribute may be inferred from Visualization 1, which shows how the $k_{\perp}\omega$ -spectrum of Fig. 5 (b) develops during propagation from $z = 71.50$ mm to $z = 73.00$ mm (see Supplementary Material). Note that all spectra in this animation are normalized to the peak of the first frame: $I(k_{\perp}, \omega)$ at $z = 71.50$ mm. The inset of Fig. 5 (b) shows that, as nonlinear effects occur, energy is partially diffracted away, but to a greater extent spreads toward $k_{\perp} = 0$, corresponding to pulse energy that is redirected parallel to the propagation axis. In other words, the conical, inward-directed pulse is partially drawn into a filament. Subsequently, the on-axis plasma locally defocuses the converging annulus, diffracting energy into non-annular, Gaussian-like pulse fronts (see Fig. 5 (a) with a mind to Fig. 3 (a)). In addition, Fig. 5 (b) shows that energy is also distributed to higher frequency components by the plasma. Kerr self-phase modulation indeed broadens the pulse spectrum as its intensity increases, but it does so more symmetrically. Components beyond ~ 4 rad/fs are purely attributable to plasma-induced spectral blueshifting [55].

The morphology of maximum free carrier densities, i.e. ionization tracks, is expected to depend on incident pulse energy and pre-chirp, since these quantities affect the space and time shape of a pulse as it approaches the nonlinear focus, and therefore, how the light-matter dynamics unfold there. In this study, we hold constant the parameters that would affect the degree of radial chirp (e.g. w_{inc} , incident pulse spectral width, grating attributes, etc.), as well as the numerical aperture of the focusing geometry. We thus restrict this study to a two-dimensional

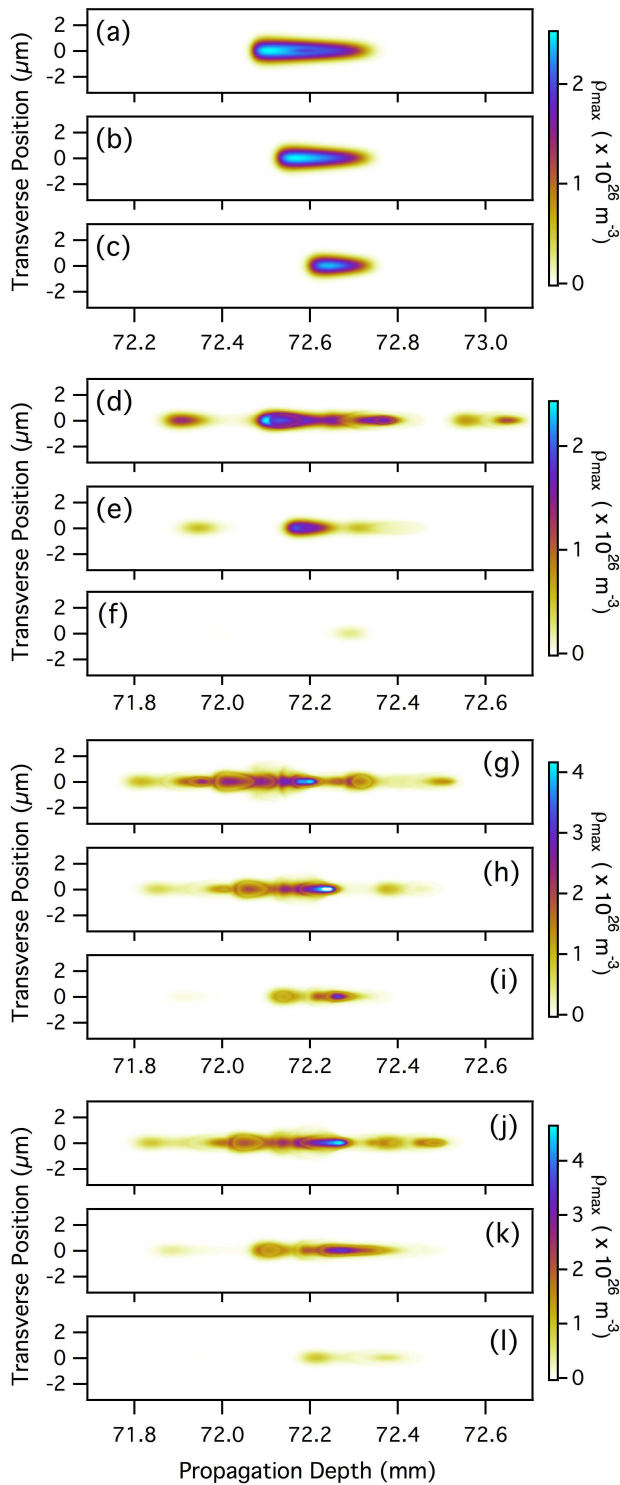


Fig. 6. Ionization tracks from pulses with various pre-chirp and energy. Each three-plot sequence of free carrier densities $\rho_{\max}(r, z)$ corresponds to the sequence of pulse energies: $0.9 \mu\text{J}$, $0.7 \mu\text{J}$, $0.5 \mu\text{J}$. Each color map is set by the peak of the $0.9\text{-}\mu\text{J}$ data. (a)-(c) GB with $\tau_0 = 40$ fs. (d)-(f) RCA with $b_2 = 1700$ fs² ($\tau_0 = 239$ fs). (g)-(i) RCA with $b_2 = 1100$ fs² ($\tau_0 = 158$ fs). (j)-(l) RCA with $b_2 = 900$ fs² ($\tau_0 = 131$ fs). Note that for case (h), the color map is saturated on-axis at $z \sim 72.2$ (displayed as white), where ρ_{\max} reaches a peak value of $4.53 \times 10^{26} \text{ m}^{-3}$.

parameter space with dimensions of 1) pulse energy and 2) pre-chirp value.

Shown in Fig. 6 are ionization tracks from RCA pulses with various pre-chirp and energy, with GB results for comparison. Each three-plot sequence of free carrier densities $\rho_{\max}(r, z)$ corresponds to the sequence of pulse energies: $0.9 \mu\text{J}$, $0.7 \mu\text{J}$, $0.5 \mu\text{J}$. The three pre-chirps in terms of b_2 are 1700 fs^2 (panes (d)-(f)), 1100 fs^2 (panes (g)-(i)), and 900 fs^2 (panes (j)-(l)). These data reflect the oscillatory nature of energy deposition to the propagation axis and the dependence of track morphology on the relative coincidence of temporal and spatial foci in the presence of optical nonlinearities, and in the context of this focusing geometry (numerical aperture, w_{inc}).

The pre-chirp parameter adds an additional control over how the filament develops via SSTF, Kerr and plasma nonlinearities, etc. It has been shown that this parameter affects the longitudinal tilt out of the transverse plane of the intensity distribution at the focus in SSTF systems [28, 29]. In our simulations we find that, as the Bessel-like distribution develops in the focal region (prior to the onset of strong nonlinear effects), the longitudinal dependence of its spatial wing is likewise pre-chirp-dependent (data not shown), with lower pre-chirps producing a spatial wing lagged slightly in time relative to larger pre-chirps. Thus, in addition to controlling the overall pulse duration in the focal region, the pre-chirp affects the longitudinal arrangement of energy as it is deposited to the $r = 0$ symmetry axis during the nonlinear focusing. As a result, varying the pre-chirp has a significant effect on the morphology of ionization tracks. A case in point is shown in pane (h). Here, the color map is set by the data in pane (g), and is saturated in pane (h). This means that, despite an energy decrease by 22.2%, and having a common pre-chirp, the peak of $\rho_{\max}(r, z)$ increases by 10%. This counterintuitive result points to a non-trivial abstract surface in the energy/pre-chirp parameter space. Following a curved path in this parameter space that corresponds to, for example, the Fig. 6 pane sequence (e) \rightarrow (i) \rightarrow (k), the morphology transitions from one more similar to the GB result in pane (c) to a morphology approaching what would be expected from a typical Bessel-Gauss beam. Bessel-Gauss beams are characterized by better localization in r but delocalization in z [23]. Intermediate between these two points is a result (pane (i)) with peak structure that is well-localized in both r and z . To reiterate: As the pre-chirp parameter is swept past that value which gave optimal SSTF in a linear simulation (nonlinearities switched off), the ionization track acquires an all-around better-localized peak structure provided the energy is decreased by $\sim 25\%$. These features indicate that variable space-time focusing of radially chirped femtosecond pulses may provide a useful addition to the laser materials processing toolbox.

5. DISCUSSION

We now examine a special case in more detail by further comparing the $0.5\text{-}\mu\text{J}$ RCA with $b_2 = 1100 \text{ fs}^2$ ($\tau_0 = 158$ fs) with its GB counterpart. While the case of the $0.5\text{-}\mu\text{J}$ GB is completely analogous to and effectively summarized by Fig. 3 panes (a)-(c), the RCA dynamics are more complex. The pulse development during propagation from $z = 71.80$ mm to $z = 72.55$ mm is depicted in Visualization 2 (see Supplementary Material), which animates the rt -space intensity associated with the ionization track shown in Fig. 8 (b). We note that, in this animation, intensity values in excess of $50 \text{ TW}/\text{cm}^2$ saturate the color map (displayed as white), with intensity reaching a peak of $128 \text{ TW}/\text{cm}^2$

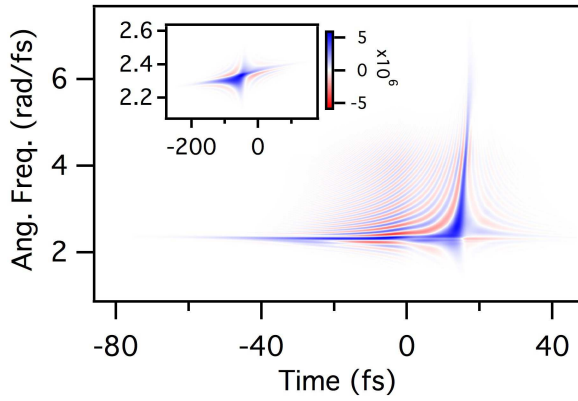


Fig. 7. Wigner-Ville distributions of the on-axis electric field for the RCA at $z = 72.27$ mm corresponding to Fig. 8 (b), and the GB corresponding to Fig. 8 (a) at $z = 72.70$ mm (inset).

at $z = 72.26$ mm. A notable feature of this progression is the direction of the temporal migration of the on-axis intensity spike during the strongest ionization: it is lagged as opposed to advanced as in the GB case.

Further insight may be gained from time-frequency representations of particular on-axis fields. The Wigner-Ville distribution is the following time-frequency representation of an isolated wave packet (pulse):

$$W(t, \omega) = \int_{-\infty}^{\infty} E(t + \frac{\tau}{2}) E^*(t - \frac{\tau}{2}) e^{-i\omega\tau} d\tau, \quad (12)$$

where $E(t)$ is the analytic signal that can be constructed in practice from a real waveform by Fourier transforming, zeroing the negative frequency components, and inverse Fourier transforming. We note that this distribution is unique in that it does not involve a choice of gate function, is efficiently computed using Fourier transforms, and retains the property that time- and frequency-marginals give immediately the time-domain and spectral intensities, respectively [57, 58]. In other words, not only is the time-arrangement of frequencies revealed in such a way that wave-optical interference is preserved, but to the extent that an image plot can be integrated at a glance, exact time-domain and spectral intensities are represented, unadorned by any of the averaging/convolution procedures commonly employed in the context of time-frequency analysis.

As the action of the current density $J(r, t)$ is essentially confined on-axis, we calculate the Wigner-Ville distribution of on-axis electric fields for particular z -positions to provide insight into the plasma blue-shifting, which is pronounced in the RCA case and follows established trends with respect to dependence on pulse energy (see Fig. 3 in Ref. [55]). Shown in Fig. 7 are Wigner-Ville representations of the on-axis electric fields for cases GB (inset) and RCA. These data show that a plasma blue-shift to $\sim 2.5\omega_0$ arises late in the pulse development, which is early in terms of the current density development. This frequency shift is a signature of a free carrier density that spikes abruptly in time [56]. In addition, these shifted components are on the order of 10^{-3} of the peak spectral intensity. Therefore, experimental detection is feasible. In Fig. 8, the corresponding ionization tracks are compared. The RCA case is characterized by a more structured plasma channel. It possesses a peak structure that is arguably subwavelength in the radial dimension, and is better localized overall as compared with the GB case.

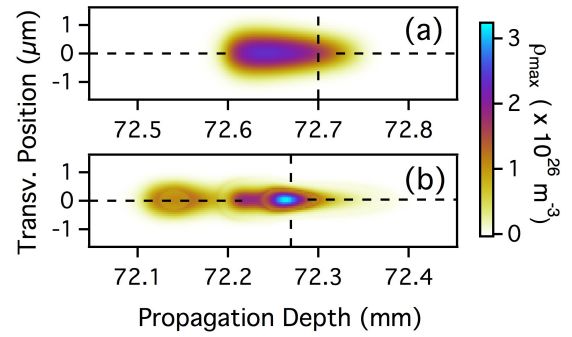


Fig. 8. Closer comparison of 0.5- μ J ionization tracks for (a) GB with $\tau_0 = 40$ fs and (b) RCA with $b_2 = 1100$ fs² ($\tau_0 = 158$ fs). The color map is set by the peak of the RCA data. Dashed lines indicate the positions corresponding to Wigner-Ville distributions shown in Fig. 7. The rt -space intensity development associated with the track in pane (b) is depicted in Visualization 2 (see Supplementary Material).

6. CONCLUSIONS

We present a model for the action of concentric gratings on laser pulses and numerically propagate the space-time-focusing field resulting from propagation through a conjugating pair of these gratings in fused silica glass. These simulations reveal the impact of familiar dynamical pulse propagation effects on the focusing of these unconventional pulses, and suggest novel approaches to laser machining of solids. In particular, ionization tracks in the bulk show more localized (sub-micron) ionization peaks when compared to those of a Gaussian pulse of the same energy and numerical aperture. We note that the numerical aperture used in this paper was chosen as a compromise between computational size constraints and the tight-focusing conditions common to laser machining. Similarly, the degree of radial chirp is limited by our choice of annulus size, and could be increased significantly in the laboratory. SSTF is not, in itself, a singular result of light-matter interactions but rather is a fundamental wave propagation phenomenon that happens to be useful for the tailoring of optical effects in matter. Therefore, we expect that our results may be extrapolated to larger radial chirps and the larger numerical apertures that often occur in the context of laser micro- and nano-machining.

APPENDIX A: HANKEL TRANSFORM

In cylindrical coordinates the transform $E(k_{\perp}, t) \xrightarrow{\text{HT}} E(r, t)$ is accomplished via the discrete Hankel transform [43–45]:

$$H_{ij} = \frac{2}{\alpha_{N+1}} \frac{J_0(\alpha_j \alpha_j / \alpha_{N+1})}{J_1^2(\alpha_j)}. \quad (13)$$

In other words,

$$E[r[i], t] = \sum_{j=1}^N H_{ij} E[k_{\perp}[j], t]. \quad (14)$$

Here, α_i is the i^{th} zero of the Bessel function J_0 and N is the size of arrays $r[i] = R_{\text{max}} \frac{\alpha_i}{\alpha_{N+1}}$ and $k_{\perp}[j] = \frac{\alpha_j}{R_{\text{max}}}$ to which the electric field array is referenced. The matrix H_{ij} is self-reciprocal for

large N , so that the inverse transform is performed by multiplication by the same matrix. We note that the above discrete transform is symmetrized for a numerical algorithm in which the scaling between forward and backward transforms cancels. The transforms that maintain Parseval's relation are:

$$f[i] = \frac{\alpha_{N+1}}{R_{\max}^2} \sum_{j=1}^N H_{ij} F_0[j] \quad (15)$$

$$F_0[j] = \frac{R_{\max}^2}{\alpha_{N+1}} \sum_{i=1}^N H_{ji} f[i].$$

APPENDIX B: LENS TRANSFORMATION

The lens is inserted into the beam path at a particular z -position by multiplying the field at that z -position $\tilde{E}(r, \omega)$ by the phase

$$\exp \left\{ i \frac{\omega}{c} [n(\omega)L(r) + (d_0 - L(r))] \right\} \quad (16)$$

with lens thickness function $L(r) = d_0 - \frac{r^2}{2} \left(\frac{1}{R_1} - \frac{1}{R_2} \right)$ to correspond to a thin lens approximation [48]. Here, d_0 is the lens center thickness, $n(\omega)$ is the frequency dependent refractive index of the lens material as described by a Sellmeier equation, R_i are the radii of curvature, and the surrounding medium is treated as vacuum. The lens material used in this paper is fused silica, with linear losses and all nonlinearities are neglected. A simple biconvex lens of nominal focal length f is obtained by setting $R_1 = -R_2 = 2f(n_0 - 1)$, where n_0 is the refractive index at the pulse center frequency. The phase quadratic in r and roughly linear in ω produces the curved phase and pulse fronts of the field transmitted by the lens. Spatially dependent group velocity dispersion and chromaticity of the lens are thus accounted for to infinite dispersion order.

We note that, as a practical consideration, a compensating phase $\exp \left\{ -i \frac{\omega}{v_g} L(r_0) \right\}$, must be applied during this transformation to shift the entire waveform in time and thus keep the pulse centered in the retarded time frame window. Here, r_0 is approximately equal to the transverse position of the spatial component to be kept centered, and $v_g = \left(\frac{dk}{d\omega} \Big|_{\omega_0} \right)^{-1}$ is the group velocity of the pulse in the lens material. For a typical on-axis intensity distribution, r_0 would be taken to be 0, but this is not the case for an annular spatial distribution.

Funding. Air Force Office of Scientific Research (AFOSR), (FA9550-13-1-0069).

REFERENCES

1. A. Couairon and A. Mysyrowicz, "Femtosecond filamentation in transparent media," *Physics Reports* **441**, 47–189 (2007).
2. M. Kolesik, E. M. Wright, and J. V. Moloney, "Dynamic nonlinear x waves for femtosecond pulse propagation in water," *Phys. Rev. Lett.* **92**, 253901 (2004).
3. M. Kolesik, E. M. Wright, and J. V. Moloney, "Interpretation of the spectrally resolved far field of femtosecond pulses propagating in bulk nonlinear dispersive media," *Opt. Express* **13**, 10729–10741 (2005).
4. S. Tzortzakis, L. Sudrie, M. Franco, B. Prade, A. Mysyrowicz, A. Couairon, and L. Bergé, "Self-guided propagation of ultrashort laser pulses in fused silica," *Phys. Rev. Lett.* **87**, 213902 (2001).
5. W. Liu, S. Petit, A. Becker, N. Aközbeke, C. Bowden, and S. Chin, "Intensity clamping of a femtosecond laser pulse in condensed matter," *Optics Communications* **202**, 189–197 (2002).
6. K. Yamada, W. Watanabe, T. Toma, K. Itoh, and J. Nishii, "In situ observation of photoinduced refractive-index changes in filaments formed in glasses by femtosecond laser pulses," *Opt. Lett.* **26**, 19–21 (2001).
7. L. Sudrie, A. Couairon, M. Franco, B. Lamouroux, B. Prade, S. Tzortzakis, and A. Mysyrowicz, "Femtosecond laser-induced damage and filamentary propagation in fused silica," *Phys. Rev. Lett.* **89**, 186601 (2002).
8. Z. Wu, H. Jiang, Q. Sun, H. Yang, and Q. Gong, "Filamentation and temporal reshaping of a femtosecond pulse in fused silica," *Phys. Rev. A* **68**, 063820 (2003).
9. N. Nguyen, A. Salimonia, S. Chin, and R. Vallée, "Control of femtosecond laser written waveguides in silica glass," *Applied Physics B* **85**, 145–148 (2006).
10. K. Mishchik, C. D'Amico, P. K. Velpula, C. Maclair, A. Boukenter, Y. Ouerdane, and R. Stoian, "Ultrafast laser induced electronic and structural modifications in bulk fused silica," *Journal of Applied Physics* **114**, 133502 (2013).
11. Q. Sun, H. Asahi, Y. Nishijima, N. Murazawa, K. Ueno, and H. Misawa, "Pulse duration dependent nonlinear propagation of a focused femtosecond laser pulse in fused silica," *Opt. Express* **18**, 24495–24503 (2010).
12. S. Onda, W. Watanabe, K. Yamada, K. Itoh, and J. Nishii, "Study of filamentary damage in synthesized silica induced by chirped femtosecond laser pulses," *J. Opt. Soc. Am. B* **22**, 2437–2443 (2005).
13. A. Couairon, L. Sudrie, M. Franco, B. Prade, and A. Mysyrowicz, "Filamentation and damage in fused silica induced by tightly focused femtosecond laser pulses," *Phys. Rev. B* **71**, 125435 (2005).
14. H. Guo, H. Jiang, Y. Fang, C. Peng, H. Yang, Y. Li, and Q. Gong, "The pulse duration dependence of femtosecond laser induced refractive index modulation in fused silica," *Journal of Optics A: Pure and Applied Optics* **6**, 787 (2004).
15. J. F. Herbstan and A. J. Hunt, "High-aspect ratio nanochannel formation by single femtosecond laser pulses," *Opt. Express* **18**, 16840–16848 (2010).
16. P. Polynkin, M. Kolesik, J. V. Moloney, G. A. Siviloglou, and D. N. Christodoulides, "Curved plasma channel generation using ultraintense airy beams," *Science* **324**, 229–232 (2009).
17. P. Polynkin, M. Kolesik, A. Roberts, D. Faccio, P. D. Trapani, and J. Moloney, "Generation of extended plasma channels in air using femtosecond Bessel beams," *Opt. Express* **16**, 15733–15740 (2008).
18. P. Polesana, M. Franco, A. Couairon, D. Faccio, and P. Di Trapani, "Filamentation in Kerr media from pulsed Bessel beams," *Phys. Rev. A* **77**, 043814 (2008).
19. C. Ament, P. Polynkin, and J. V. Moloney, "Supercontinuum generation with femtosecond self-healing airy pulses," *Phys. Rev. Lett.* **107**, 243901 (2011).
20. A. Chong, W. H. Renninger, D. N. Christodoulides, and F. W. Wise, "Airy-Bessel wave packets as versatile linear light bullets," *Nature Photonics* **4**, 103–106 (2010).
21. M. K. Bhuyan, P. K. Velpula, J. P. Colombier, T. Olivier, N. Faure, and R. Stoian, "Single-shot high aspect ratio bulk nanostructuring of fused silica using chirp-controlled ultrafast laser Bessel beams," *Applied Physics Letters* **104**, 021107 (2014).
22. J. Amako, D. Sawaki, and E. Fujii, "Microstructuring transparent materials by use of nondiffracting ultrashort pulse beams generated by diffractive optics," *J. Opt. Soc. Am. B* **20**, 2562–2568 (2003).
23. M. K. Bhuyan, F. Courvoisier, P.-A. Lacourt, M. Jacquot, L. Furfaro, M. J. Withford, and J. M. Dudley, "High aspect ratio taper-free microchannel fabrication using femtosecond Bessel beams," *Opt. Express* **18**, 566–574 (2010).
24. G. Zhu, J. van Howe, M. Durst, W. Zipfel, and C. Xu, "Simultaneous spatial and temporal focusing of femtosecond pulses," *Opt. Express* **13**, 2153–2159 (2005).
25. D. Oron, Y. Silberberg, "Spatiotemporal coherent control using shaped, temporally focused pulses," *Opt. Express* **13**, 9903–9908 (2005).
26. F. He, H. Xu, Y. Cheng, J. Ni, H. Xiong, Z. Xu, K. Sugioka, and K. Midorikawa, "Fabrication of microfluidic channels with a circular cross section using spatiotemporally focused femtosecond laser pulses," *Opt.*

- Lett. **35**, 1106–1108 (2010).
27. R. Kammel, R. Ackermann, J. Thomas, J. Götte, S. Skupin, A. Tünnermann, and S. Nolte, "Enhancing precision in fs-laser material processing by simultaneous spatial and temporal focusing," *Light Sci. Appl.* **3**, e169 (2014).
 28. B. Zeng, W. Chu, H. Gao, W. Liu, G. Li, H. Zhang, J. Yao, J. Ni, S. L. Chin, Y. Cheng, and Z. Xu, "Enhancement of peak intensity in a filament core with spatiotemporally focused femtosecond laser pulses," *Phys. Rev. A* **84**, 063819 (2011).
 29. F. He, B. Zeng, W. Chu, J. Ni, K. Sugioka, Y. Cheng, and C. G. Durfee, "Characterization and control of peak intensity distribution at the focus of a spatiotemporally focused femtosecond laser beam," *Opt. Express* **22**, 9734–9748 (2014).
 30. M. Clerici, D. Faccio, E. Rubino, A. Lotti, A. Couairon, and P. D. Trapani, "Space-time focusing of bessel-like pulses," *Opt. Lett.* **35**, 3267–3269 (2010).
 31. D. N. Vitek, D. E. Adams, A. Johnson, P. S. Tsai, S. Backus, C. G. Durfee, D. Kleinfeld, and J. A. Squier, "Temporally focused femtosecond laser pulses for low numerical aperture micromachining through optically transparent materials," *Opt. Express* **18**, 18086–18094 (2010).
 32. D. N. Vitek, E. Block, Y. Bellouard, D. E. Adams, S. Backus, D. Kleinfeld, C. G. Durfee, and J. A. Squier, "Spatio-temporally focused femtosecond laser pulses for nonreciprocal writing in optically transparent materials," *Opt. Express* **18**, 24673–24678 (2010).
 33. E. Block, M. Greco, D. Vitek, O. Masihzadeh, D. A. Ammar, M. Y. Kahook, N. Mandava, C. Durfee, and J. Squier, "Simultaneous spatial and temporal focusing for tissue ablation," *Biomed. Opt. Express* **4**, 831–841 (2013).
 34. Y.-C. Park and S.-W. Kim, "Determination of two-dimensional planar displacement by Moiré fringes of concentric-circle gratings," *Appl. Opt.* **33**, 5171–5176 (1994).
 35. F. Xu, S. Zhou, S. Hu, W. Jiang, L. Luo, and H. Chu, "Moiré fringe alignment using composite circular-line gratings for proximity lithography," *Opt. Express* **23**, 20905–20915 (2015).
 36. A. Ilovitsh, V. Mico, and Z. Zalevsky, "Super resolved optical system for objects with finite sizes using circular gratings," *Opt. Express* **23**, 23667–23679 (2015).
 37. C. Zhou, J. Jia, and L. Liu, "Circular Dammann grating," *Opt. Lett.* **28**, 2174–2176 (2003).
 38. F. J. Wen and P. S. Chung, "Design of Circular Dammann Grating: Fabrication and Analysis", *Advances in Unconventional Lithography*, In-Tech, (2011), <http://www.intechopen.com/books/>.
 39. M. Beresna, M. Gecevičius, and P. G. Kazansky, "Ultrafast laser direct writing and nanostructuring in transparent materials," *Adv. Opt. Photon.* **6**, 293–339 (2014).
 40. E. Bricchi, J. D. Mills, P. G. Kazansky, B. G. Klappauf, and J. J. Baumberg, "Birefringent Fresnel zone plates in silica fabricated by femtosecond laser machining," *Opt. Lett.* **27**, 2200–2202 (2002).
 41. M. Kolesik, J. V. Moloney, and M. Mlejnek, "Unidirectional optical pulse propagation equation," *Phys. Rev. Lett.* **89**, 283902 (2002).
 42. A. Couairon, E. Brambilla, T. Corti, D. Majus, O. de J. Ramírez-Góngora, and M. Kolesik, "Practitioner's guide to laser pulse propagation models and simulation," *The European Physical Journal Special Topics* **199**, 5–76 (2011).
 43. H. Johnson, "An improved method for computing a discrete hankel transform," *Computer Physics Communications* **43**, 181 – 202 (1987).
 44. M. Guizar-Sicairos and J. C. Gutiérrez-Vega, "Computation of quasi-discrete hankel transforms of integer order for propagating optical wave fields," *J. Opt. Soc. Am. A* **21**, 53–58 (2004).
 45. N. Baddour and U. Chouinard, "Theory and operational rules for the discrete hankel transform," *J. Opt. Soc. Am. A* **32**, 611–622 (2015).
 46. L. V. Keldysh, "Ionization in the field of a strong electromagnetic wave," *Sov. Phys. JETP* **20**, 1307 (1965).
 47. S. Winkler, I. Burakov, R. Stoian, N. Bulgakova, A. Husakou, A. Mermillod-Blondin, A. Rosenfeld, D. Ashkenasi, and I. Hertel, "Transient response of dielectric materials exposed to ultrafast laser radiation," *Applied Physics A* **84**, 413–422 (2006).
 48. J.-C. Diels, and W. Rudolph, *Ultrashort Laser Pulse Phenomena*, (Academic press, 2006), 2nd ed., Chap. 2.
 49. N. Baddour, "Application of the generalized shift operator to the hankel transform," *SpringerPlus* **3**, 246 (2014).
 50. B. M. Levitan, G. L. Litvinov (originator), "Generalized displacement operators", *Encyclopedia of Mathematics*, <http://www.encyclopediaofmath.org/>.
 51. O. E. Martinez, "Grating and prism compressors in the case of finite beam size," *J. Opt. Soc. Am. B* **3**, 929–934 (1986).
 52. M. C. Hutley, *Diffraction gratings*, Techniques of Physics (Academic Press, London, 1982), Chap. 2.
 53. M. A. Porras, R. Borghi, and M. Santarsiero, "Suppression of dispersive broadening of light pulses with bessel-gauss beams," *Optics Communications* **206**, 235 – 241 (2002).
 54. H. E. Hernández-Figueroa, M. Zamboni-Rached, and E. Recami, *Localized Waves*, (John Wiley and Sons, 2007), Chap. 2.
 55. S. C. Rae and K. Burnett, "Detailed simulations of plasma-induced spectral blueshifting," *Phys. Rev. A* **46**, 1084–1090 (1992).
 56. J. R. Gulley and W. M. Dennis, "Ultrashort-pulse propagation through free-carrier plasmas," *Phys. Rev. A* **81**, 033818 (2010).
 57. F. Hlawatsch and P. Flandrin, *The Wigner distribution: Theory and Applications in Signal Processing*, W. Mecklenbräuker and F. Hlawatsch, eds. (Elsevier, Amsterdam, 1997).
 58. B. Boashash, "Note on the use of the wigner distribution for time-frequency signal analysis," *Acoustics, Speech and Signal Processing, IEEE Transactions on* **36**, 1518–1521 (1988).